ACS Photonics

Open Access

pubs.acs.org/journal/apchd5

Article

High-NA 2D Image Edge Detection Using Tamm Plasmon Polaritons in Few-Layer Stratified Media

Published as part of ACS Photonics special issue "Rising Stars in Photonics".

Bernardo S. Dias and Jorik van de Groep*

Cite This: https://doi.org/10.1021/acsphotonics.4c01667

Read Online

ACCESS | Metrics & More | Article Recommendations | Supporting Information

ABSTRACT: Analog optical computing with nanophotonic devices has emerged as a promising solution to the need for ultrafast computation with low power consumption. Several key mathematical operations, including spatial derivatives for edge detection, have recently been demonstrated. However, these initial approaches are typically characterized by a small numerical aperture (NA), strong polarization dependence, narrow operational bandwidths, or the need for complex nanofabrication procedures. Here, we demonstrate how a very simple 7-layer thin-film stack provides dual-channel, high efficiency, polarization-independent 2D edge detection with a numerical aperture approaching 0.9, by leveraging the intrinsic properties of Tamm plasmon polariton resonances. By engineering the resonant decay rates, we propose simple design rules for the layer stack to achieve high-efficiency edge detection with a NA that matches the desired spatial resolution. Using this, we experimentally demonstrate edge detection of micrometer-scale targets with a bandwidth reaching up to 10 nm, enabling operation under filtered, unpolarized, and low-coherence illumination from a halogen lamp. Our results push optical image edge detection toward a wider range of practical applications, including high-resolution microscopy.

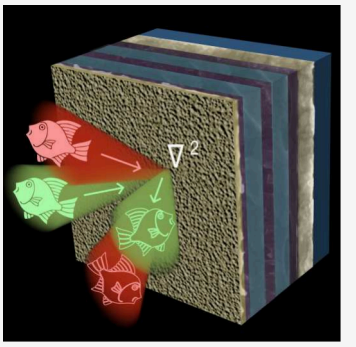

KEYWORDS: *nanophotonics, optical image processing, edge detection, Tamm plasmon polariton, optical computing*

INTRODUCTION

Recent developments in emerging technologies such as artificial intelligence decision making, virtual/augmented reality, and autonomous driving push the need for new image processing solutions. The increasing demand on existing hardware exposes limitations not only in terms of processing speed, but also in energy consumption.[1] In response to these challenges, analogue optical computation has seen a recent resurgence facilitated by highly compact nanophotonic coatings. Such metasurfaces enable ultrafast mathematical operations to be performed fully in the optical domain without the need for electronics, leading to very low energy consumption while offering facile integration with existing imaging technologies. Using various nanostructured coatings, a range of mathematical operations has already been demonstrated, including 1D first- and second-order derivatiation,[2,3] 2D Laplacian operation,[4−7] integration,[8] phase contrast imaging,[9] and image classification.[10−12]

A key process in image processing is edge detection, as it forms one of the first steps in object recognition algorithms with applications in autonomous driving,[13] virtual reality,[14] and facial recognition.[15] One possible implementation of edge detection in analogue optical computation uses a second-order derivative of the image brightness in the spatial domain, enhancing sharp variations (edges) and suppressing the background. For 2D operation, the Fourier transform of the second-order differential of $f(x, y)$ gives

$$\mathcal{F}(\nabla^2 f(x, y)) = -(k_x^2 + k_y^2)\mathcal{F}(f(x, y)) \quad (1)$$

where $\mathcal{F}$ is the Fourier transform operator and k_x and k_y are the spatial frequencies in the x and y directions, respectively. Equation 1 implies that a parabolic filter in the k-space performs a Laplacian operation on an image, as demonstrated in several devices.[3,5] Nevertheless, various limitations have been identified for these initial demonstrations, such as polarization dependence, small numerical apertures (NA), small operational bandwidths, and challenging fabrication processes.[2,3,16] As such, more recent works have focused on solving these issues to provide more practical implementations of edge detection.[5−7,17] Most notably, recent experimental[18] and theoretical[19] reports explore the possibility of performing edge detection up to near-unity NAs with polarized light only. However, neither demonstrated experimentally the high-NA capabilities of these devices. Furthermore, refs 4 and5 show

Received: September 2, 2024
Revised: November 18, 2024
Accepted: November 19, 2024

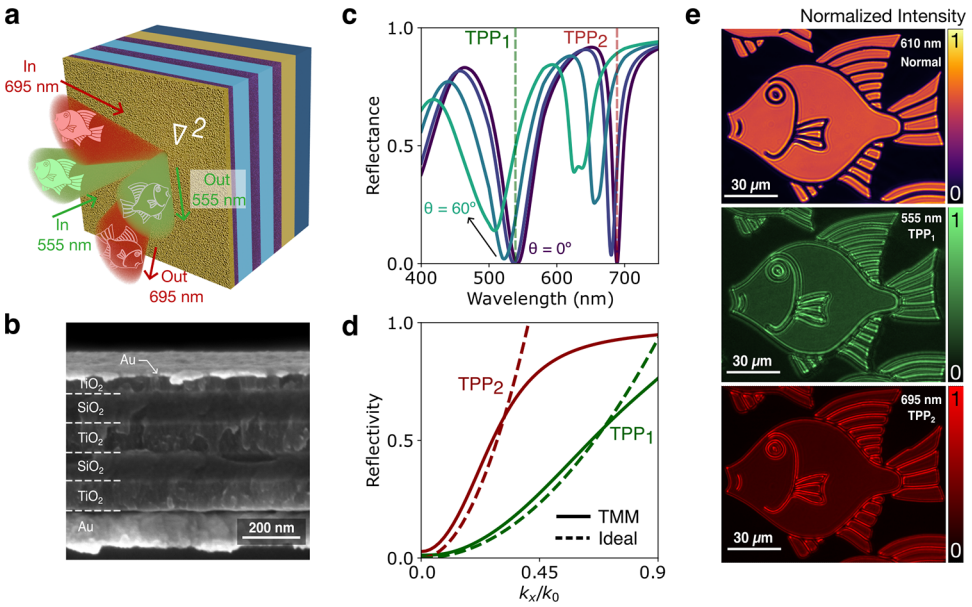

Figure 1. 2D edge detection with TPPs in a simple layer stack. (a) Schematic of the concept: a photonic crystal sandwiched between two Au layers supports two TPPs at different wavelengths (555 (green) and 695 nm (red)). At these wavelengths, the reflected images show strongly enhanced edges for edge detection. (b) Scanning electron microscopy (SEM) image of a cross section of the fabricated device. (c) Calculated reflectance spectrum of the layer stack for unpolarized light for varying angles of incidence, showing the resonance shift for increasing angles, calculated with the transfer-matrix method (TMM). (d) Calculated reflectivity (r) using the TMM for the operation wavelengths as a function of the in-plane wavevector (solid). The ideal ideal parabolic response is also shown (dashed). (e) Demonstration of full-2D edge detection with the fabricated device. The original target image is part of M.C. Eschers' lithography Metamorphose II (1939).

broadband and polarization-independent operation with NAs up to 0.315 and 0.350, respectively. However, these promising examples still require nanopatterning or layer stacks with up to 40 thin films[16] and do not yet meet the NA needed for edge detection on (sub)micron scale features.

Here, we propose Tamm plasmon polaritons (TPPs) in a simple 7-layer stratified medium as a promising solution for polarization-independent 2D image edge detection, with an operational NA approaching 0.9. TPPs are electromagnetic modes supported at the interface between a 1D periodic nonhomogeneous medium and a metal layer,[20,21] and find applications in optical sensors,[22,23] filters,[24] and optical cavities for strong coupling.[25,26] Interestingly, TPPs inherently exhibit large field enhancements, polarization degeneracy up to large angles of incidence, and a parabolic dispersion within the light cone, allowing the direct excitation from air.[20] We leverage these intrinsic properties to design a 7-layer device that supports two TPP modes at different wavelengths (thus, providing two distinct edge detection channels). We provide rational design rules to optimize the NA of the device to the desired spatial resolution and experimentally demonstrate highly efficient 2D edge detection on both large and small targets down to 1 μm. For such small features, we combine the different NAs of the two channels to study the role of the NA in the performance. Finally, we show that edge detection is preserved for an operational bandwidth up to 10 nm, even when illuminated with a filtered, noncoherent halogen lamp. Importantly, our thin-film stack can be fabricated over large areas using simple physical vapor deposition methods,[16,27] without the need for expensive nanopatterning methods. Altogether, our results provide a uniquely simple structure for 2D differentiation with unprecedented high NA, pushing analog image processing toward a wider range of practical applications.

2D EDGE DETECTION WITH TAMM PLASMON POLARITONS

Figure 1a presents a schematic of the concept of dual-channel 2D image edge detection using Tamm Plasmons. A simple layer stack composed of a two-period distributed Bragg reflector (DBR) capped by Au layers on both sides supports two TPP modes, providing two edge detection channels in reflection. Figure 1b shows a scanning electron microscopy image of a cross section of the fabricated device. The multilayer structure of the DBR is clearly visible between the top (27 nm thick) and bottom (100 nm thick) Au layers. The latter also functions as a backreflector. At both DBR-Au interfaces, a TPP mode is supported, which carve distinct dips in the calculated reflectance spectrum (Figure 1c). For normal incidence (θ = 0°), the two critically coupled TPP modes reach R = 0 at free-space wavelengths λ = 555 nm (TPP_1) and λ = 695 nm (TPP_2), which defines the operation wavelengths of the two edge detection channels. On the other hand, increasing the angle of incidence blue-shifts the resonant dips and increases the reflectance as the modes are no longer critically coupled. As such, under normal incidence, light is fully absorbed by the structure, while light incident at increasing angles will experience an increasing reflectivity. As the in-plane projection, $k_{||}$, of the free-space wavevector, k_0, is associated with in-plane spatial frequencies, this optical response enables filtering of the low frequency components of images that are projected onto the device. Figure 1d shows the variation in the reflectivity, $|r| = \sqrt{R}$, for the TPP wavelengths as a function of the incident in-plane wavevector, $k_{||}/k_0$. Both TPPs closely follow the ideal quadratic dependence (eq 1) up to $k_{||}/k_0$ = 0.7 (TPP_1) and $k_{||}/k_0$ = 0.3 (TPP_2), which defines the maximum numerical aperture, NA = $k_{||}/k_0$, for the operation. Nevertheless, note that both modes exhibit a continued increase in reflectivity for larger wavevectors. The

https://doi.org/10.1021/acsphotonics.4c01667
ACS Photonics XXXX, XXX, XXX−XXX

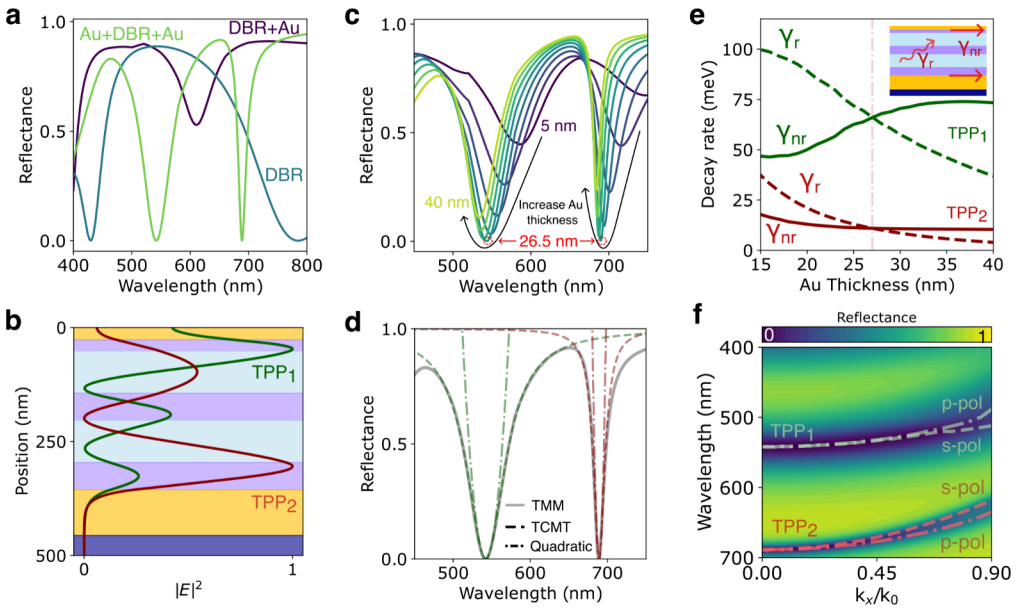

Figure 2. Design of layer stack for edge detection with TPPs. (a) TMM calculated reflectance of the bare DBR (blue), DBR with Au back reflector (purple) and complete film stack (green), showing the band gap, formation of TPP_2, and both TPPs, respectively. (b) Normalized field intensity profiles of both TPP modes under excitation with *s* polarized light, showing field concentrations close to the metal−DBR interfaces. (c) TMM calculations of the layer stack for varying thickness of the top Au layer showed critical coupling of both modes for 26.5 nm. (d) Fitting of eq 3 and its Taylor expansion to the calculated TPP spectrum, showing good agreement with TCMT and the quadratic approximation around resonance. (e) Plot of the extracted radiative (dashed) and nonradiative (solid) decay rates of both TPPs as a function of Au thickness, demonstrating critical coupling ($\gamma_{rad} = \gamma_{nr}$) at the same Au thickness of 26.5 nm. (f) Calculated dispersion relation of the optimized device under unpolarized light (color), showing the parabolic behavior of both resonances. The dashed lines represent the dispersion of the TPP modes under *s* and *p* polarized light.

reflectivity of TPP_1 follows the parabolic trend up to NA = 0.9 within a 15% error, while for TPP_2 it stabilizes around 0.5. In practice, the parabolic reflectivity results in effective filtering of the low frequency components but reflection of the high frequency components. This enhances the rapid spatial intensity variations in the reflected image and enables edge detection of any projected image. As we will show, the maximum NA of the mode plays a key role in the resolution of the edge detection images.

To demonstrate the two channel edge detection using TPPs, we use optical lithography to fabricate an ∼100 μm-sized fish target in Cr on a SiO_2 substrate. Figure 1e shows the image formed at a nonresonant wavelength (λ = 610 nm) where the device acts as a mirror (top). The bright parts correspond to light transmitted through the target. On the other hand, for both TPP operation wavelengths (bottom), a clear enhancement of the edges is observed−most notably in the areas where high spatial frequencies are involved (e.g., the fish's scales). Crucially, edge detection is characterized by a large contrast with respect to the background and works for all orientations of the edges. Figure 1e thus demonstrates that TPPs supported by a simple layer stack enable a full 2D Laplacian operation, obtaining a clear edge detection.

NANOPHOTONIC DESIGN OF EDGE DETECTION WITH TPPS

TPPs modes are supported between a DBR and a metal layer and are characterized by field enhancement in the first layer near the interface.[20,21] To rationalize the design of the thin film stack for edge detection, we start by analyzing the resonant conditions of TPPs. By considering a DBR−metal interface and applying the method of virtual interfaces, it can be shown that the resonant condition is given by[20]

$$r_{DBR} r_M e^{2iknd} = 1 \quad (2)$$

where r_{DBR} and r_M are the DBR and metal Fresnel reflection coefficients, k is the wavevector, n is the high refractive index (RI) of the last DBR layer, and d its thickness. Considering the mode is placed in the band gap region of the DBR and the metal−dielectric reflectivity is also very high, $|r_{DBR}| \approx |r_M| \approx 1$, eq 2 shows that the TPP mode follows from a constructive interference condition at the layer between the DBR and the metal.[28] As such, the TPP can be considered as a cavity mode, where light is trapped and amplified between the high reflectivity of both the DBR and the metal. Equation 2 also shows that TPPs are inherently polarization independent (degenerate) since the absolute values of r_{DBR} and r_M are very similar for both polarizations up to large angles. Indeed, the polarization splitting for both resonances is visible only at high angles (60°) in Figure 1c, showing that the TPPs enable a polarization-independent Laplacian operation up to very high angles.

To design the film stack supporting two orthogonal channels, we start by designing a DBR with a wide bandgap by choosing materials with a high RI contrast (SiO_2 and TiO_2, $\Delta n \approx 0.8$).[29] The thicknesses of the materials are set for the central wavelength of the bandgap (λ_c = 552 nm) to be positioned in the visible range according to the quarter wavelength condition $n_{TiO_2} d_{TiO_2} = n_{SiO_2} d_{SiO_2} = \lambda_c/4$, where n_{TiO_2} and n_{SiO_2} are the RIs of TiO_2 and SiO_2, respectively, d_{TiO_2} and d_{SiO_2} are the unit cell layer thicknesses. The resulting DBR shows a high reflectance across the visible spectral range (Figure 2a), which ensures that two independent modes with sufficient detuning can be accommodated within a single bandgap.

https://doi.org/10.1021/acsphotonics.4c01667
ACS Photonics XXXX, XXX, XXX−XXX

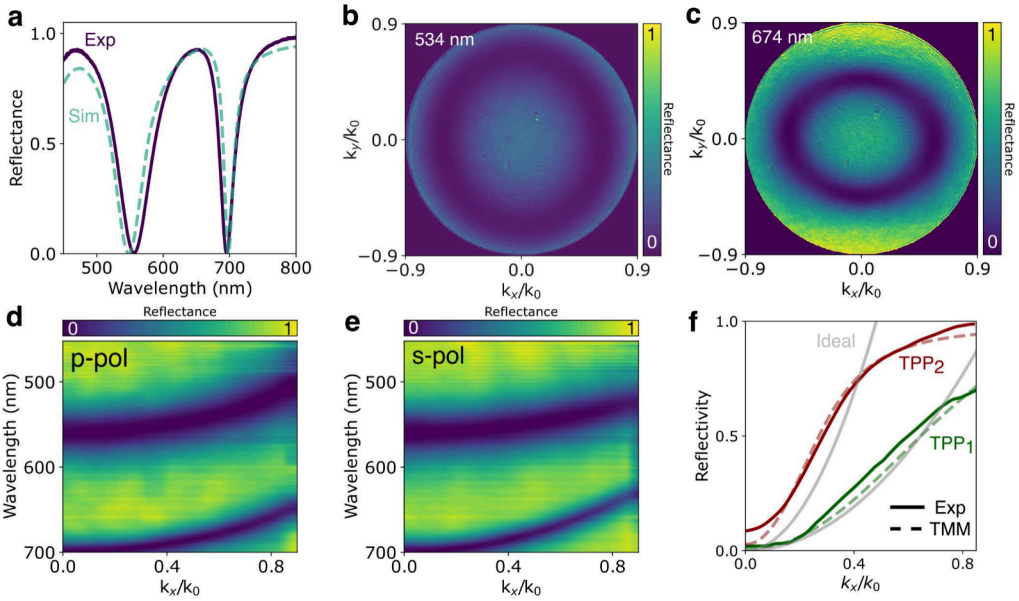

Figure 3. Experimental spectroscopic measurements of the fabricated layer stack. (a) Reflectance spectrum under normally incident unpolarized light (solid) and comparison with TMM calculations (dashed). (b, c) BFP measurements of TPP_1 (b) and TPP_2 (c) at slightly detuned wavelengths. The outer circle originates from NA = 0.9 of the microscope objective. (d, e) Experimentally measured dispersion curves for *s*- (d) and *p*-polarized light (e). The lifting of the polarization degeneracy is visible at large *k*-values. (f) Extracted reflectivity curves at the operation wavelengths (solid) and the corresponding TMM calculations (dashed). The ideal parabolic response is also shown (gray).

Next, we employ a thick (opaque) back reflector, creating the DBR−Au interface that supports TPP_2. See Figure 2a,b for the resulting reflection spectrum and mode profile, respectively. At the top interface, we then placed a thin, partially transparent Au film that plays two crucial roles. First, at this interface TPP_1 is supported (Figure 2b). To guarantee strong detuning of both TPPs, the top TiO_2 layer, which determines the constructive interference condition (eq 1) for TPP_1, is thinned down to 25 nm. Second, the thickness of this gold layer directly controls the coupling strength of both TPPs to the free space. Figure 2c shows the reflectance as the thickness of the top Au layer is varied to explore where the critical coupling condition is fulfilled. We observe a high overall reflectance background (caused by the DBR bandgap) with the two distinct dips due to the TPP modes. For increasing Au thickness (starting at 5 nm), the reflectance of both modes drops rapidly downward until critical coupling is achieved (for t_{Au} = 26.5 nm), followed by an increase.

To unravel the underlying mechanism responsible for the trends seen in Figure 2c, we use temporal coupled mode theory (TCMT) to study the interplay between the radiative (γ_{rad} − reflection) and nonradiative decay rates (γ_{nr} − absorption in the Au layers). The TPPs can be considered as independent cavity modes between two high reflectivity mirrors, the DBR and the metal layer. Therefore, the reflectance of each mode can be modeled as a single port resonator:[30,31]

$$R(\omega) = \frac{(\gamma_{rad} - \gamma_{nr})^2 + (\omega - \omega_0)^2}{(\gamma_{rad} + \gamma_{nr})^2 + (\omega - \omega_0)^2} \quad (3)$$

where ω is the angular frequency and ω_0 is the resonant frequency. Equation 3 shows that reaching zero reflectance at resonance ($R(\omega_0) = 0$), which is essential for edge detection to filter the low frequency background, requires the critical coupling condition $\gamma_{rad} = \gamma_{nr}$.[32,33] The TCMT (eq 3) describes well the optical response of the device around resonance, as highlighted by the fit in Figure 2d. By employing a fitting routine based on our TMM calculations (see Methods), we extract γ_{rad} and γ_{nr} as a function of the top Au layer thickness (Figure 2e). We observe that, for TPP_2, both γ_{rad} and γ_{nr} are smaller than for TPP_1, as expected from its smaller line width. The lower γ_{nr} is explained by both the lower absorption of Au at λ = 695 nm (TPP_2) compared to that at λ = 555 nm (TPP_1), as well as the smaller field overlap with the Au for TPP_2 (Figure 2b). On the other hand, the smaller γ_{rad} can be rationalized by the smaller field amplitude at the interface of the device and thus smaller modal overlap with free space radiation compared to TPP_1. Nevertheless, for both modes, Figure 2e confirms the crossing of the decay rates ($\gamma_{rad} = \gamma_{nr}$) at the same Au thickness, confirming the double critically coupled resonance for t_{Au} = 26.5 nm. For both modes, we observe that for thinner Au the system is overcoupled ($\gamma_{rad} > \gamma_{nr}$), while a thicker Au layer leads to undercoupling ($\gamma_{rad} < \gamma_{nr}$).[30]

We now study the dispersion relation of TPPs for the optimized film stack (Figure 2f). The dispersion for unpolarized light (background) is overlaid with the resonance wavelengths for both *s*- and *p*-polarized light. We observe a clear parabolic trend in the dispersion of both TPPs with small splitting only at larger angles. Both properties are reported characteristics for TPP modes[20] and highly beneficial for 2D edge detection.

RATIONAL DESIGN RULES FOR THE NA IN EDGE DETECTION

Building on the insights provided by the TCMT analysis, we can now derive a direct link between the resonance decay rates, γ_{rad} and γ_{nr}, and the desired NA for an envisioned application in edge detection. We start by performing a Taylor expansion of eq 3 near the resonance condition, obtaining up to third order an approximation to the reflectance as $R(\omega) \approx \frac{(\omega - \omega_0)^2}{(\gamma_{rad} + \gamma_{nr})^2}$,

https://doi.org/10.1021/acsphotonics.4c01667
ACS Photonics XXXX, XXX, XXX−XXX

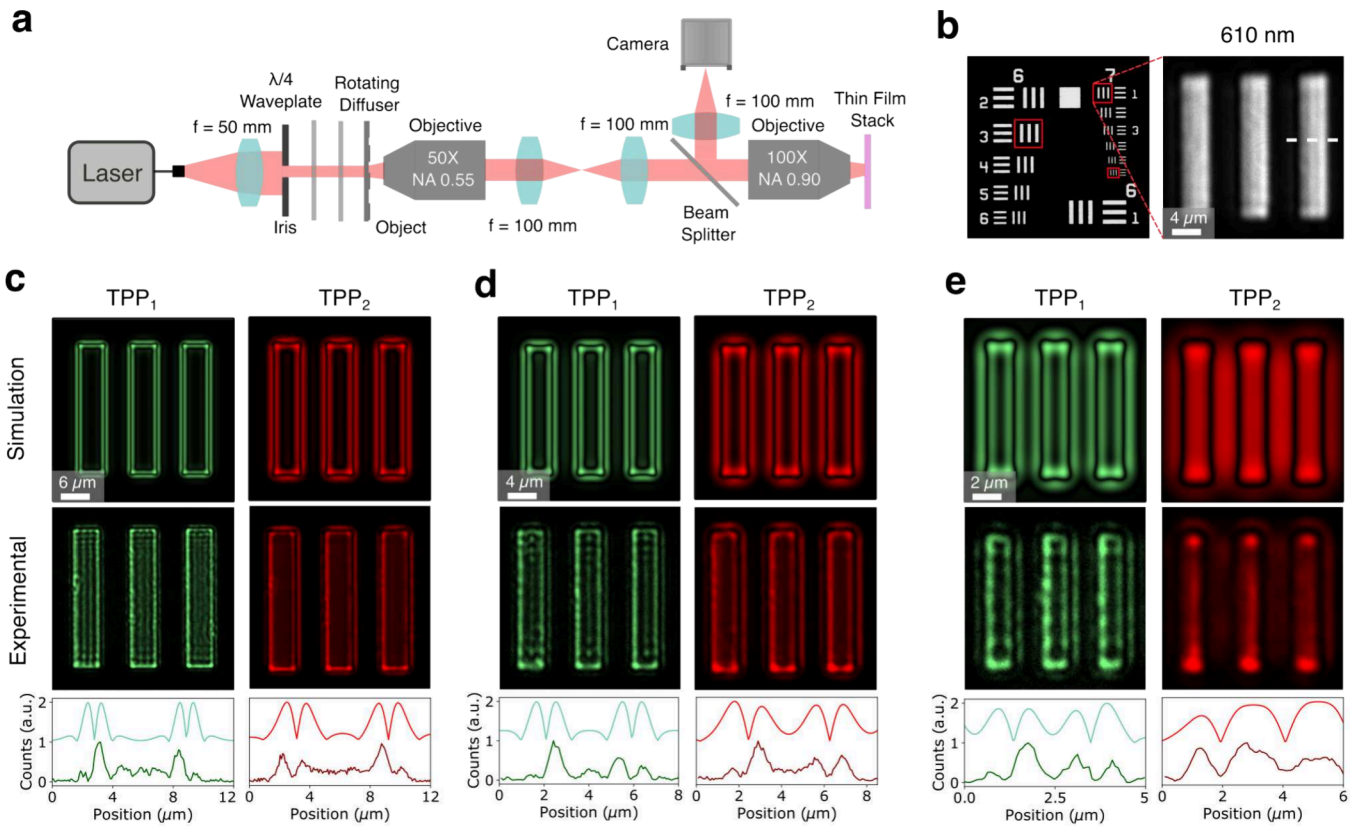

Figure 4. Experimental edge detection using Tamm Plasmon Polaritons. (a) Experimental setup used for edge detection. (b) Image of the three bar target used (USAF 1951 resolution target), measured at a nonresonant wavelength of 610 nm. The dashed line indicates the cross sections taken in (c)−(e). (c−e) Simulated (top) and experimental (middle) results for Group 6 Element 3 (c, 6 μm, 80.6 lp/mm), Group 7 Element 3 (d, 4 μm, 128 lp/mm), and Group 7 Element 6 (e, 2 μm, 228 lp/mm). The objects are further demagnified 2× by the objectives. Results are shown for TPP_1 (left) and TPP_2 (right). Representative cross cuts are also shown (bottom), which are offset for the sake of clarity.

which is also fitted with good agreement around resonance in Figure 2d. Next, by modeling the TPP dispersion relation as $\omega(k_{x,y}) = \omega_0 + ak_{x,y}^2$ with fitting constant a, we can rewrite the Taylor expanded equation as $R(k_{x,y}) = \left(\frac{a}{(\gamma_{rad}+\gamma_{nr})}\right)^2 k_{x,y}^4$, implying

$$|r(k_{x,y})| = (R(k_{x,y}))^{1/2} = \frac{a}{(\gamma_{rad}+\gamma_{nr})}k_{x,y}^2 \quad (4)$$

Equation 4 highlights how the parabolic dispersion of TPPs offers the ideal response function $|r(k_{x,y})| \propto k_{x,y}^2$ needed for the Laplacian operation. Furthermore, eq 4 also provides a direct handle on the desired operation NA, which can be controlled through the modal loss rates. As also discussed in a previous work,[5] we emphasize how the control of the edge detection NA is important for different applications: for small objects, a low NA places limitations on the edge detection resolution, while a NA that is too large for a given object results in small efficiencies, causing low signal-to-noise ratios between the background and the edges. Assuming the proposed device is to be designed to perform ideal edge detection of objects with a maximum spatial frequency ν and wavevector $k_{obj} = 2\pi\nu$, and since $|r(k_{obj})| = 1$ for optimal edge detection, we can calculate the optimal condition

$$\nu = \frac{1}{2\pi}\left(\frac{\gamma_{rad}+\gamma_{nr}}{a}\right)^{1/2} \quad (5)$$

This establishes a direct connection between the object's spatial frequency and the TPP parameters and shows that the smallest feature in the image dictates the optimal loss rates of the TPP resonance to reach the desired NA. Using this analysis, the higher NA of TPP_1, as observed in Figure 1d, is directly explained by the larger loss rates demonstrated in Figure 2e, which gives rise to a slower parabolic trend (eq 4) and a higher resolvable spatial frequency (eq 5).

SPECTROSCOPIC CHARACTERIZATION

To experimentally validate the k-dependent response of our structure, we employ reflection spectroscopy. Figure 3a compares the experimental and calculated reflectance spectra for unpolarized light under normal incidence. A very good agreement between the measured and TMM-calculated spectra is observed, which confirms the dual-resonant behavior of the sample. Both resonances show near-zero reflectance due to critical coupling. To measure the dispersion relation and spatial frequency response of the device, we employ back focal plane (BFP) measurements of the light reflected from the layer structure. Representative BFP images near both resonance wavelengths show a characteristic ring-shaped dip in reflectance for both polarizations (Figure 3b,c). The approximate circular shape in the k_x−k_y plane shows that a full-2D Laplacian operation can be realized. For wavelengths further detuned from resonance, we observe a slight effect of the polarization splitting for TPP_2 (Figure 3c). Since this

https://doi.org/10.1021/acsphotonics.4c01667
ACS Photonics XXXX, XXX, XXX−XXX

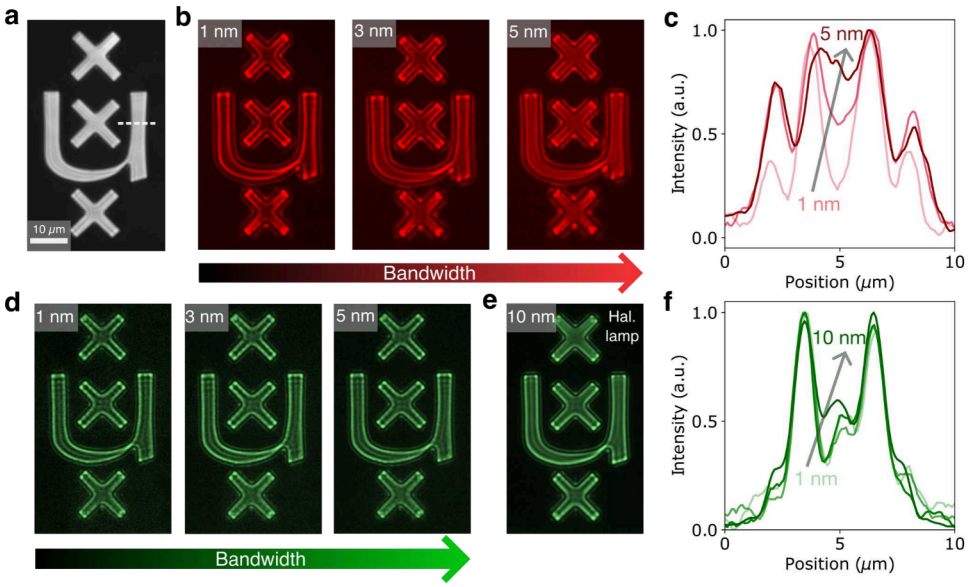

Figure 5. Bandwidth and coherence tolerances of TPP-based edge detection. (a) Original image of the institution's logo target. The cross section used for (c) and (f) is shown as a dashed line. (b) Edge detection of the institution's target with TPP_2 for increasing (laser) illumination bandwidth from 1 to 5 nm. (c) Line cuts through the edge detection images in (b). (d) Edge detection with TPP_1 for increasing the (laser) illumination bandwidth from 1 to 5 nm. (e) Edge detection with TPP_1 using a halogen lamp and a 10 nm bandpass filter. (f) Line cuts through the edge detection images in (d) and (e).

corresponds to large angles of incidence, it does not significantly affect the performance of the device.

From the collected BFP measurements, we extracted the full dispersion curves for both polarizations by taking line cuts along the $k_{x,y} = 0$ axes for a range of wavelengths. The resulting dispersion diagrams clearly confirm the parabolic trend for both TPPs (Figures 3d,e) and show very good agreement with the calculated dispersion (Figure 2f). The polarization splitting at high k-values is manifested as slightly different slopes around $k_{x,y}/k_0 \sim 0.9$.

Finally, these dispersion diagrams enable the extraction of the $|r(k_{x,y})| = \sqrt{R(k_{x,y})}$ by taking horizontal cross cuts from Figure 3d,e at the operation wavelengths for edge detection. The resulting experimental reflectivity curves show excellent agreement with the TMM calculations (Figure 3f) with a very good approximation of the optimal parabolic dispersion. Although TPP_1 is characterized by full suppression at $k_{\|} = 0$ through critical coupling, TPP_2 displays a small reflectivity at normal incidence, which will contribute to a small background in the processed images.

EXPERIMENTAL EDGE DETECTION

The two TPP modes supported by our structure exhibit a different numerical aperture, implying different edge-detection performance depending on the object's spatial frequency. For larger objects (lower spatial frequencies), such as in Figure 1e, TPP_2 shows brighter edges due to the steeper slope in Figure 3f. This larger efficiency highlights that for large objects the TPP NA should be matched (i.e., not too high) to maximally enhance the edges of the smallest feature in the image (eq 5).

To further investigate the effect of different working NA's for small targets, we use a standard USAF 1951 resolution target along with an experimental setup with demagnification capabilities (Figure 4a). The demagnification allows us to obtain responses for even smaller objects than those in the resolution target, pushing the limits of the TPP performance. The object is illuminated with light from a supercontinuum laser coupled to an acousto-optic tunable filter, providing a line width of ~1 nm. Light passes through an iris, a $\lambda/4$ waveplate (to achieve equal parts of s- and p-polarized light), and a rotating diffuser to reduce the spatial coherence and speckle formation in the captured images. Next, the object is demagnified using both objectives of mismatched magnification (50 and 100×), providing a 2× increase in the objects spatial frequencies before projecting it on the sample. A 1:1 relay system is employed between the objectives to allow decoupling between real and reciprocal space, achieving higher image quality. Finally, a beamsplitter sends the reflected image to a tube lens to project it onto a monochrome CMOS camera.

An original image of the three-bar target obtained at a nonresonant wavelength of 610 nm is shown in Figure 4b. By changing the group and element of the target, we assess the edge detection capabilities using bars ranging from 6 to 2 μm in the cross section (which are further demagnified 2× by the objectives). The experimental edge detection results are shown in Figure 4c–e. To provide a meaningful comparison, we simulate the expected images using Fourier filtering of the target image, taking into account the TPP response function from Figure 1d (see Methods for details). For all targets, a characteristic double line in edge detection is observed, caused by the second-order nature of the Laplacian operation. To emphasize this, cross sections of the experimental and simulated data are also shown (bottom). Although TPP_1 and TPP_2 show very similar responses for the larger target (c), significant differences are observed for the smallest target (e).

To understand this, we can derive a maximum spatial frequency that could be resolved for a given TPP NA: $\nu_{max} = NA/\lambda$, where λ is the operation wavelength. From this, we find $\nu_{max}^{TPP1} = 625$ lp/mm (resolution of 0.8 μm) and $\nu_{max}^{TPP2} = 214$ lp/mm (resolution of 2.3 μm), reflecting the effect of the higher NA of TPP_1. For the largest object $\nu = 80.6$ lp/mm (Figure 4c), both TPPs are able to fully resolve the object's edges as expected. Note that for TPP_1 we also observe two lines inside

https://doi.org/10.1021/acsphotonics.4c01667
ACS Photonics XXXX, XXX, XXX−XXX

the bars caused by diffractive effects, which are also reported in previous works.[6] Similar results are observed for the middle target (Figure 4d, ν = 128 lp/mm), where both TPPs resolve the object, but the double line is now more visible. However, for the smallest target (Figure 4e), where ν = 228 lp/mm, TPP_2 is no longer able to provide a clear edge detection image, as expected from $\nu_{obj} > \nu_{max}$. These results are in very good agreement with the simulations, where the same effect is observed. These results underline the importance of high-NA edge detection for smaller objects. Furthermore, for the case of TPP_1, we demonstrate edge detection of a 1 μm width bar (accounting for the demagnification), demonstrating the high-NA capabilities of this mode and paving the way for edge detection of submicrometer objects in microscopy applications.

The test targets used so far all exhibit very large contrasts and sharp edges. To demonstrate the relevance of our design to more challenging and realistic scenario's, we also present edge detection on biological cells that display very small intensity contrast and finite phase contrast (Supporting Information, Figure S2).

OPERATIONAL BANDWIDTH AND COHERENCE

For practical purposes, the ability to perform optical edge detection without narrow-band (and highly coherent) laser illumination is essential to facilitate integration with existing imaging systems.[5] In resonance-based edge detection, the operation bandwidth correlates directly with the NA of the resonance, which we have related to the resonance loss rates. The key challenge lies in the divergence from the required parabolic response for detuned wavelengths, which contributes to undesired background intensities. For our TPP design, the response of the device slightly detuned from resonance is still approximately parabolic, promising a larger operational bandwidth for TPP_1 in particular due to its higher NA.

To explore the device's performance with increasing bandwidth, we use a target of our institution's logo (Figure 5a) and illuminate it with increasing bandwidth Γ using our coherent supercontinuum laser. Figure 5b presents the results for TPP_2. Clear edge detection of the target is observed for Γ = 1 nm, but the edges become increasingly indistinguishable from the background as Γ approaches 5 nm, as corroborated by the cross sections (Figure 5c). For TPP_1 on the other hand, the edges remain to be strongly pronounced up to Γ = 5 nm (Figure 5d,f) due to the larger resonance line width. To further test the limit toward real world applications, we replace the supercontinuum laser with a halogen lamp combined with a 10 nm full-width half-maximum (fwhm) bandpass filter centered at 560 nm. This allows us to test edge detection with an extended source (low spatial coherence) and in a more practical scenario. As a result of the high NA of TPP_1, clear edge detection is still observed (Figure 5e,f), demonstrating how high resolution edge detection of small objects is possible even with low coherence, unpolarized, broadband light.

DISCUSSION

Our results demonstrate how TPPs in few-layer stratified media provide an easy platform to achieve edge detection that is particularly tunable in terms of operational NA. Designing the layer stack to achieve critical coupling provides strong suppression of the background, while simultaneous engineering of the resonance Q-factor determines the NA. Although such design routines have been discussed in previous works,[4,5] it was pointed out that these realizations suffered from low intensity throughput and high polarization anisotropies. TPPs thus appear as an excellent candidate for this approach, facilitated by the large reflectance contrast that leads to high efficiencies and the polarization degeneracy up to large angles. Furthermore, we show that the intrinsic parabolic dispersion of TPPs provides an ideal k-space filter response up to large NAs.

The design control provided by this framework is of particular relevance to the field of microscopy, where small objects are commonly studied. Although previous works have highlighted how a NA that is too large leads to low efficiency edge detection on large objects,[5] we also demonstrate limitations in the opposite case. When the operational NA is too low, edge detection on small targets is compromised due to a lack of resolution. We conclude that, within a certain range, care should be taken to match the NA to the object's spatial frequencies, maximizing edge detection efficiency while obtaining a well-resolved image.

In contrast with previous work, our edge detection operates in reflection rather than transmission. Despite the fact that this approach may come at the expense of slightly more complex integration with existing imaging setups, we emphasize a specific performance advantage. By reducing the cavity to a single port resonator, we show that critical coupling (and, thus, efficient suppression of the background) is achievable by engineering of γ_{nr}. While absorption losses are undesirable in transmission mode (due to lower efficiencies and higher background contribution), here we leverage Au absorption as an important design feature that enables matching of the resonant decay rates.

CONCLUSION

In summary, we demonstrate how the intrinsic parabolic dispersion of Tamm Plasmon Polaritons provides a remarkably facile and efficient opportunity for 2D edge detection using analogue optical computing, without the need for nano-patterning. Using temporal coupled mode theory, we design a dual-resonant layer structure with two distinctly different NA's approaching up to 0.9, and provide rational design rules to optimize the NA to the desired spatial resolution. Our experiments demonstrate the near-perfect optical properties of the simple layer structure as well as highly efficient 2D edge detection on both large and small targets. We carefully assess the role of the NA and highlight the need to match the NA to the target's spatial frequencies. Finally, we show that a large NA offered by TPPs provides a high tolerance to increased illumination bandwidths, and that edge detection is achieved even with filtered illumination from a noncoherent halogen lamp. These results demonstrate that TPPs provide a unique and facile solution for edge detection in, for example, microscopy applications, where both small and large targets need to be resolved.

METHODS

Sample Fabrication. The multilayer stack samples are fabricated using electron beam physical vapor deposition (Polyteknik Flextura M508 E) on a cleaned Si substrate. For Au deposition, a deposition rate of 0.5 Å/s is used, resulting in a smooth film. For SiO_2 and TiO_2, a deposition rate of 2 Å/s is used. Deposition of TiO_2 is done using a Ti_3O_5 precursor under a O_2 atmosphere at 2.5 × 10^{-8} mbar.

https://doi.org/10.1021/acsphotonics.4c01667
ACS Photonics XXXX, XXX, XXX−XXX

The materials and final thicknesses of the layer stack are (from substrate to top): Au (100 nm)−TiO_2 (60 nm)−SiO_2 (92 nm)−TiO_2 (60 nm)−SiO_2 (92 nm)−TiO_2 (25 nm)−Au (26.5 nm).

TMM Calculations. TMM calculations are performed using the TMM package available for Python.[34] The refractive indices of Au and SiO_2 are taken from literature.[35,36] For TiO_2, the refractive index is measured using spectroscopic ellipsometry on the as-deposited material (VB-400 J.A. Woollam).

Edge Detection Simulations. To simulate the bar targets, an ideal (binary) image of the three bars was designed. The correct size of the image is determined by matching the number of pixels in the bars to the spatial frequency of the corresponding USAF 1951 target. First, we calculate the Fourier transform of the image and apply a low-pass filter simulating the effect of the cutoff caused by the system's first objective (NA = 0.55). Next, we apply the parabolic filter obtained from the TMM simulations for each TPP in the Fourier space, simulating the effect of light reflecting on the thin film stack. Lastly, an inverse Fourier transform is applied to obtain the resulting edge detection image.

Decay Rate Calculations. We employ a fitting routine described in ref 33 to analyze the coupling rates for each TPP. In this procedure, a Lorentzian line shape is fitted to each resonance in the TMM spectra (providing the total decay rate γ) and to a similar set of spectra obtained by setting the imaginary part of the Au permittivity to zero (neglecting losses in the system), which allows the extraction of γ_{rad}. Finally, the nonradiative decay is determined by $\gamma_{nr} = \gamma - \gamma_{rad}$.

Spectroscopic Measurements. Measurement of reflectance spectrum and BFP images are both performed using a Witec α300R confocal Raman microscope. For the reflectance spectrum, a Zeiss EC Epiplan 20× (NA = 0.4) was used with a halogen lamp as the light source. For this measurement, a Ag mirror (Thorlabs PF10-03-P01) was used as a reference, and the angular range of incidence was minimized by closing the aperture stop on the Köhler illumination. For the BFP measurements, a 100× Zeiss EC Epiplan-Neofluar (NA = 0.9) microscope objective is used with a supercontinuum laser (NKT SuperK Extreme EXW-12) coupled to an acousto-optical tunable filter (AOTF, SuperK Select, 1 nm line width) as light source. Here, the same Ag mirror is also used as a reference. By sweeping wavelengths with the laser and taking line cuts at $k_{x,y} = 0$ in the BFP images, both the dispersion relation and the parabolic $|r(k_x/k_0)|$ curves are extracted.

Experimental Setup for Edge Detection. For the setup shown in Figure 4, Thorlabs AC254-100-A-ML achromatic doublet lenses (with antireflection coating from 400 to 700 nm) are used in the setup. The $\lambda/4$ achromatic waveplate (Thorlabs AQWP05M-580) has a working range of 400−800 nm. For the objectives, a Zeiss 50× LD EC Epiplan-Neofluar (NA = 0.55) is used for object collection, and a 100× Zeiss EC Epiplan-Neofluar (NA = 0.9) is used for projection on the film stack, providing a 2× demagnification. These objectives are chosen for their almost matching size of their physical BFP aperture, which is essential to preventing clipping in the reciprocal space. Finally, the image is projected on a monochrome camera (IDS U3-3880CP-M-GL).

For edge detection with an incoherent broadband source, a halogen lamp (Thorlabs OSL2 Fiber Illuminator) along with a 10 nm bandwidth filter centered at 560 nm (Thorlabs FBH560-10) was used. Here, light from a halogen lamp is coupled into a fiber bundle (effective core diameter of 6.4 mm) and onto the optical system, replacing the single mode fiber as the source in Figure 4a. For this measurement, the $\lambda/4$ waveplate and rotating diffuser were removed from the setup.

To obtain the edge detection images, an image of a target is first acquired using the camera software. We then block the path between the beamsplitter and the 100× objective to collect a background image. Subtraction of the two enables background correction of small reflections from the beamsplitter.

■ ASSOCIATED CONTENT

Data Availability Statement

A full replication package, including all data and analysis scripts, is freely available on 10.6084/m9.figshare.27798342.v1.

Supporting Information

The Supporting Information is available free of charge at https://pubs.acs.org/doi/10.1021/acsphotonics.4c01667.

BFP measurements of both TPPs at resonance. Edge detection of a phase object consisting of a human buccal epithelial cell (PDF)

■ AUTHOR INFORMATION

Corresponding Author

Jorik van de Groep − *Van der Waals-Zeeman Institute, Institute of Physics, University of Amsterdam, Amsterdam 1098 XH, The Netherlands;* orcid.org/0000-0003-3033-8005; Email: j.vandegroep@uva.nl

Author

Bernardo S. Dias − *Van der Waals-Zeeman Institute, Institute of Physics, University of Amsterdam, Amsterdam 1098 XH, The Netherlands*

Complete contact information is available at: https://pubs.acs.org/10.1021/acsphotonics.4c01667

Notes

The authors declare no competing financial interest.

■ ACKNOWLEDGMENTS

This work was funded by the Open Technology Program of the Dutch National Science Foundation (NWO), Grant Number 19486. We gratefully acknowledge T. Bauer for scientific discussions, A. Lambertz for the SEM imaging, F. Koenderink for lending us the rotating diffuser, T. Veeken for the ellipsometry data, and R. Dziobek Garrett for the language screening.

■ REFERENCES

(1) Jones, N. How to stop data centres from gobbling up the world's electricity. *Nature* **2018**, *561*, 163−166.

(2) Zhu, T.; Zhou, Y.; Lou, Y.; Ye, H.; Qiu, M.; Ruan, Z.; Fan, S. Plasmonic computing of spatial differentiation. *Nat. Commun.* **2017**, *8*, 15391.

(3) Cordaro, A.; Kwon, H.; Sounas, D.; Koenderink, A. F.; Alù, A.; Polman, A. High-Index Dielectric Metasurfaces Performing Mathematical Operations. *Nano Lett.* **2019**, *19*, 8418−8423.

(4) Zhou, Y.; Zheng, H.; Kravchenko, I. I.; Valentine, J. Flat optics for image differentiation. *Nat. Photonics* **2020**, *14*, 316−323.

(5) Cotrufo, M.; Arora, A.; Singh, S.; Alù, A. Dispersion engineered metasurfaces for broadband, high-NA, high-efficiency, dual-polarization analog image processing. *Nat. Commun.* **2023**, *14*, 7078.

(6) Cotrufo, M.; Sulejman, S. B.; Wesemann, L.; Rahman, M. A.; Bhaskaran, M.; Roberts, A.; Alù, A. Reconfigurable image processing metasurfaces with phase-change materials. *Nat. Commun.* **2024**, *15*, 4483.
(7) Swartz, B. T.; Zheng, H.; Forcherio, G. T.; Valentine, J. Broadband and large-aperture metasurface edge encoders for incoherent infrared radiation. *Science Advances* **2024**, *10*, eadk0024.
(8) Cordaro, A.; Edwards, B.; Nikkhah, V.; Alù, A.; Engheta, N.; Polman, A. Solving integral equations in free space with inverse-designed ultrathin optical metagratings. *Nat. Nanotechnol.* **2023**, *18*, 365−372.
(9) Ji, A.; Song, J.-H.; Li, Q.; Xu, F.; Tsai, C.-T.; Tiberio, R. C.; Cui, B.; Lalanne, P.; Kik, P. G.; Miller, D. A. B.; Brongersma, M. L. Quantitative phase contrast imaging with a nonlocal angle-selective metasurface. *Nat. Commun.* **2022**, *13*, 7848.
(10) Lin, X.; Rivenson, Y.; Yardimci, N. T.; Veli, M.; Luo, Y.; Jarrahi, M.; Ozcan, A. All-optical machine learning using diffractive deep neural networks. *Science* **2018**, *361*, 1004−1008.
(11) Bai, B.; Li, Y.; Luo, Y.; Li, X.; Çetintaş, E.; Jarrahi, M.; Ozcan, A. All-optical image classification through unknown random diffusers using a single-pixel diffractive network. *Light: Science & Applications* **2023**, *12*, 69.
(12) Zheng, H.; Liu, Q.; Zhou, Y.; Kravchenko, I. I.; Huo, Y.; Valentine, J. Meta-optic accelerators for object classifiers. *Science Advances* **2022**, *8*, eabo6410.
(13) Quoc Thai, P.; Duc Tri, H.; Van Ga, B.; Van Binh, P. Application of Edge Detection Algorithm for Self-Driving Vehicles. *2022 7th National Scientific Conference on Applying New Technology in Green Buildings (ATiGB)* **2022**, 225−228.
(14) Liu, J.; Chen, D.; Wu, Y.; Chen, R.; Yang, P.; Zhang, H. Image Edge Recognition of Virtual Reality Scene Based on Multi-Operator Dynamic Weight Detection. *IEEE Access* **2020**, *8*, 111289−111302.
(15) Dong, J.; He, J.; Wang, H. Edge Detection of Human Face. *2021 IEEE International Conference on Computer Science, Electronic Information Engineering and Intelligent Control Technology (CEI)* **2021**, 596−601.
(16) Liu, Y.; Huang, M.; Chen, Q.; Zhang, D. Single planar photonic chip with tailored angular transmission for multiple-order analog spatial differentiator. *Nat. Commun.* **2022**, *13*, 7944.
(17) Deng, M.; Cotrufo, M.; Wang, J.; Dong, J.; Ruan, Z.; Alù, A.; Chen, L. Broadband angular spectrum differentiation using dielectric metasurfaces. *Nat. Commun.* **2024**, *15*, 2237.
(18) Wesemann, L.; Panchenko, E.; Singh, K.; Della Gaspera, E.; Gómez, D. E.; Davis, T. J.; Roberts, A. Selective near-perfect absorbing mirror as a spatial frequency filter for optical image processing. *APL Photonics* **2019**, *4*, 100801.
(19) Xue, W.; Miller, O. D. High-NA optical edge detection via optimized multilayer films. *Journal of Optics* **2021**, *23*, 125004.
(20) Kaliteevski, M.; Iorsh, I.; Brand, S.; Abram, R. A.; Chamberlain, J. M.; Kavokin, A. V.; Shelykh, I. A. Tamm plasmon-polaritons: Possible electromagnetic states at the interface of a metal and a dielectric Bragg mirror. *Phys. Rev. B* **2007**, *76*, 165415.
(21) Polo, J.; Mackay, T.; Lakhtakia, A. *Electromagnetic Surface Waves: A Modern Perspective*; Elsevier insights; Elsevier Science, 2013.
(22) Su, M.; Li, K.; Wang, C.; Wu, L.; Yang, S.; Lin, Q.; Li, Y.; Tang, L.; Zhou, R. Tamm-plasmon-polariton biosensor based on one-dimensional topological photonic crystal. *Results in Physics* **2023**, *48*, 106454.
(23) Juneau-Fecteau, A.; Savin, R.; Boucherif, A.; Fréchette, L. G. A practical Tamm plasmon sensor based on porous Si. *AIP Advances* **2021**, *11*, 065305.
(24) Liu, Q.; Zhao, X.; Li, C.; Zhou, X.; Chen, Y.; Wang, S.; Lu, W. Coupled Tamm plasmon polaritons induced narrow bandpass filter with ultra-wide stopband. *Nano Research* **2022**, *15*, 4563−4568.
(25) Lundt, N.; Klembt, S.; Cherotchenko, E.; Betzold, S.; Iff, O.; Nalitov, A. V.; Klaas, M.; Dietrich, C. P.; Kavokin, A. V.; Höfling, S.; Schneider, C. Room-temperature Tamm-plasmon exciton-polaritons with a WSe_2 monolayer. *Nat. Commun.* **2016**, *7*, 13328.
(26) Hu, J.; Yao, E.; Xie, W.; Liu, W.; Li, D.; Lu, Y.; Zhan, Q. Strong longitudinal coupling of Tamm plasmon polaritons in graphene/DBR/Ag hybrid structure. *Opt. Express* **2019**, *27*, 18642−18652.
(27) Zhang, X.; Bai, B.; Sun, H.-B.; Jin, G.; Valentine, J. Incoherent Optoelectronic Differentiation Based on Optimized Multilayer Films. *Laser & Photonics Reviews* **2022**, *16*, 2200038.
(28) Kar, C.; Jena, S.; Udupa, D. V.; Rao, K. D. Tamm plasmon polariton in planar structures: A brief overview and applications. *Optics & Laser Technology* **2023**, *159*, 108928.
(29) Yeh, P. *Optical Waves in Layered Media*; Wiley Series in Pure and Applied Optics; Wiley, 2005.
(30) Haus, H. *Waves and Fields in Optoelectronics*; Prentice-Hall series in solid state physical electronics; Prentice-Hall, 1984.
(31) Fan, S.; Suh, W.; Joannopoulos, J. D. Temporal coupled-mode theory for the Fano resonance in optical resonators. *J. Opt. Soc. Am. A* **2003**, *20*, 569−572.
(32) Piper, J. R.; Fan, S. Total Absorption in a Graphene Monolayer in the Optical Regime by Critical Coupling with a Photonic Crystal Guided Resonance. *ACS Photonics* **2014**, *1*, 347−353.
(33) Auguié, B.; Bruchhausen, A.; Fainstein, A. Critical coupling to Tamm plasmons. *Journal of Optics* **2015**, *17*, 035003.
(34) Byrnes, S. J. Multilayer optical calculations. *arXiv:1603.02720 [physics.comp-ph]* **2020**, na.
(35) Johnson, P. B.; Christy, R. W. Optical Constants of the Noble Metals. *Phys. Rev. B* **1972**, *6*, 4370−4379.
(36) Malitson, I. H. Interspecimen Comparison of the Refractive Index of Fused Silica. *JOSA* **1965**, *55*, 1205−1209.

https://doi.org/10.1021/acsphotonics.4c01667
ACS Photonics XXXX, XXX, XXX−XXX